LJMU Research Online

Chen, X, Chi, Y and Li, H

 In-process monitoring and analysis of bearing outer race way grinding based on the power signal

http://researchonline.ljmu.ac.uk/id/eprint/3328/

Article

For more information please contact researchonline@ljmu.ac.uk

In-Process Monitoring and Analysis of Bearing Outer Race Way Grinding based on the Power Signal

Yulun Chi[1] , Haolin Li[1], Xun Chen[2]

[1] College of Mechanical Engineering, University of Shanghai for Science and

Technology, Shanghai, China.

[2] General Engineering Research Institute, Liverpool John Moores University,

Liverpool L3 3AF, UK .

Corresponding author: Yulun Chi, Shanghai University for Science and Technology No516, Jungong Road Shanghai,

China. Email: chiyulun@163.com

Abstract

In production engineering, monitoring of the grinding process is critical for acquiring information on material removal, wheel performance, and workpiece quality. Here, a general model of the power signal and material removal rate is proposed to monitor the internal plunge grinding of a bearing outer race way product. Three continuous grinding cycles after dressing were used to analyse the roughing, semi-finishing, finishing and spark-out process under the same parameters. Based on the actual grinding process, a practical analysis method is applied to improve the general model to predict more accurately the power curve. Finally, estimations of grinding wheel performance and grind quality using the grinding power signal model (GPSM) coefficients are also presented. The experimental results showed that the improved power signal model is capable of solving the industrial problem of multi-stage in-feed grinding cycles and improving grind quality.

Keywords

1 Introduction

In modern industry, the internal plunge grinding process is widely used as the final finishing operation for the manufacture of precision inner bore parts. In particular, for the bearing outer race way (**BORW**) grinding process, its performance has the most significant effect on the product quality and productivity of the entire production line. Hence, many bearing manufacturing factories struggle to improve the grinding process to meet stringent requirements [1]. However, determining how to improve product quality and productivity of internal plunge grinding is frequently considered as one of the most important, complex and difficult problems. Compared to other common types of grinding, internal plunge grinding has unique characteristics regarding the spindle stiffness and cutting mechanism. To date, in an industrial environment, the internal plunge grinding quality control and productivity are primarily determined based on operator experience and trial and error [2-3]. Due to a lack of process information, it is difficult to select the best grinding cycle parameters to achieve the required workpiece tolerances while avoiding process instability. Therefore, an effective approach is needed to monitor the process and detect abnormalities in the precision internal plunge grinding system.

Effective monitoring and analysis of an internal plunge grinding process require the estimation and prediction of important process variables, such as the part quality and wheel conditions [3]. Many researchers have used different methods to conduct studies

on monitoring and analysis of the grinding process. Yongsheng Gao [4] proposed a recursive time constant estimation algorithm to detect the variation in grinding conditions indicated by the grinding system time constant. T. Warren Liao [5] presented a wavelet-based methodology for grinding wheel condition monitoring based on acoustic emission signals and achieved on average 97% clustering accuracy for grinding conditions. To predict the grinding power and the surface roughness prior to grinding, Jae-Seob Kwak [6] developed second-order response models for these tasks in the external cylindrical grinding of hardened SCM440 material and demonstrated that this approach is feasible for achieving satisfactory grinding conditions. Y. Gao [7] proposed an improved discrete system model to address partial removal and precision control problems and to investigate form error assessment in the partial removal stage. Although these methods can be achieved for the grinding process, they require interruption of the machining process and have strict demands on the environment. Most satisfactory results can only be acquired under strict experimental grinding conditions and are primarily applicable only in a laboratory setting rather than an actual production line. Eric R. Marsh [8] developed a force model based on material removal monitoring, which was shown to accurately control the grinding workpiece outer diameter, even in the presence of varied grinding conditions. In addition, Alex W. Moerlein [9] reported that the predictive capability of grinding force models can be extended to estimate the amount of time required for a workpiece to achieve its best roundness during spark-out. These research results verified that it is feasible to develop a monitoring method for material removal during

grinding based on the force sensor signal. However, a means of directly measuring the grinding force has yet to be developed due to the difficulty of installing the measuring instrument at the point of internal plunge grinding [10]. Recently, Chen Jiang et al. [11] reported an acoustic emission (AE) model based on grinding force models for the prediction of material removal from a workpiece. Their results indicated that acoustic emission measurements can be used to predict material removal during precision grinding. Besides, monitoring of the AE model was also used to calculate the on-line time constant of the dwell period and to estimate the workpiece grinding quality by predicting the minimum dwell time [12]. These findings demonstrate that the monitoring of material removal in plunge grinding is feasible for analysing and controlling the grinding quality. The main drawback of AE signals is the sensitivity variation according to the mounting position of the AE sensor [10]. Hence, it is impossible to mount the AE sensor at the same point for all machine tools to obtain the same sensitivity. Also, most studies based on monitoring material removal only focused on the infeed period and dwell period [8,9,11,12]. Hence, for an actual parts production line, a general model for the multi-infeed internal plunge grinding should be established to satisfy the specified requirements.

According to actual internal grinding processes, the spindle power is approximately proportional to the tangential grinding force, especially for small grinding wheels less than 100 mm in diameter [13-14]. Due to the ease of installation of the measuring instrument, a power sensor is often used to assess machine performance and tool condition and performing process monitoring [15]. In this study, the power signals of a

spindle during internal plunge grinding are obtained to construct a general model for a multi-infeed process. The model is used in a factory to monitor the internal plunge grinding of the bearing outer race way (**BORW**) product and analyse the different plunge infeed grinding processes. Three continuous grinding cycles after dressing were used to analyse the roughing, semi-finishing, finishing, and spark-out process under the same parameters. Based on the actual **BORW** grinding process, a useful practical method is proposed to improve the general model to more accurately predict the power curve. These findings demonstrate that the improved power signal model is capable of 1) solving the industrial problem of a multi-stage infeed grinding cycle and 2) providing the operators with a tool for analysing the grinding process and improving the grind quality.

2. Internal plunge grinding force model

Internal plunge grinding is a very weak system. As the grinding wheel grinds the workpiece, deformation is induced between the wheel and the workpiece, causing a delay between the command signal for the position and the system response [15, 16]. Occasionally, the magnitude of the deformation is not always fully appreciated, leading to difficulty in understanding the complex grinding process. Thus, a mathematical model of the internal plunge grinding process should be established to predict the deformation and analyse the grinding process.

As shown in Fig. 1, the internal plunge grinding machine structure can be simply modelled as three springs: the grinding wheel stiffness k_s, the workpiece with a linear spring of stiffness k_w, and the contact stiffness k_a between the grinding

wheel and the workpiece [16]. The overall effective stiffness k_e can be expressed by:

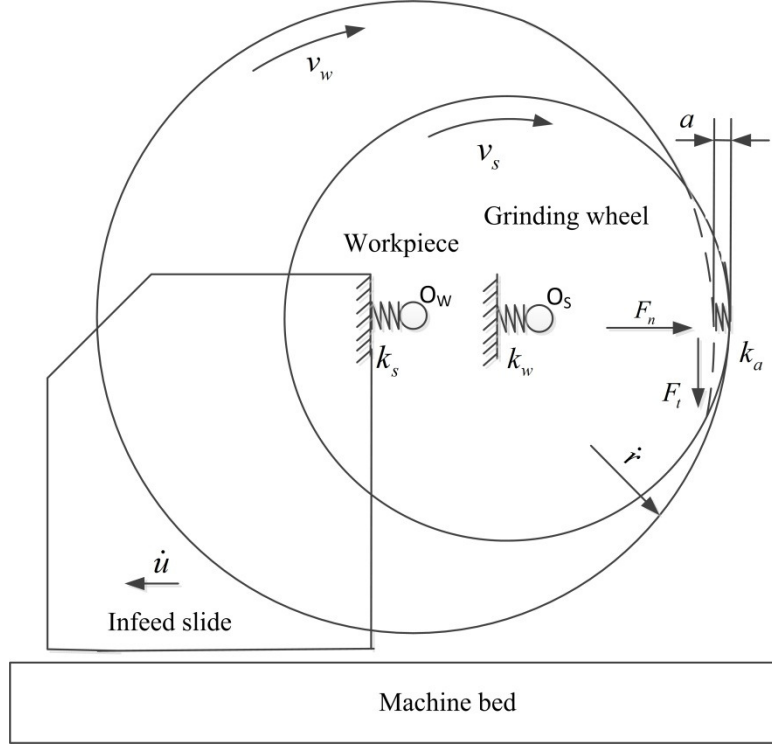$$\frac{1}{k_e} = \frac{1}{k_s} + \frac{1}{k_w} + \frac{1}{k_a}$$ (1)

Fig. 1 Internal plunge grinding model

Fig. 1 shows that when the infeed rate $\dot{u}$ is applied to the cross slide of the machine, the wheel moves towards the workpiece. The wheel grinds the workpiece, generating a grinding interface force and deflection in the grinding system [17]. To facilitate the analysis, a linear grinding force model of plunge grinding can be assumed such that the normal grinding force F_n is equal to the product of the grinding coefficient k_c and the instantaneous (not commanded) depth of cut a [8]:

$$F_n = k_c a = \frac{k_c \dot{r}}{n_w}$$ (2)

where $\dot{r}$ is the real infeed rate of the workpiece, and n_w is the rotational speed of the workpiece. The grinding coefficient k_c is used here to represent the stiffness of

the grinding action to relate the real depth of the cut to the normal grinding force. In reality, the grinding coefficient k_c is a function of the workpiece material properties as well as the grinding wheel formulation, coolant, and other parameters. Although the grinding coefficient is known to be nonlinear, a linear model is used here with acceptable accuracy [8].

It also follows that the normal grinding force F_n is proportional to the elastic deformation δ, such that:

$$\delta = \frac{F_n}{k_e} \tag{3}$$

where δ is the elastic deformation in the grinding system. As confirmed by Chen et al [16], the difference between the commanded infeed rate $\dot{u}$ and the real infeed rate $\dot{r}$ can be attributed to the change in radial elastic deflection δ in the grinding system:

$$\dot{u} - \dot{r} = \delta \tag{4}$$

By combining equations (2), (3) and (4), a control equation of the grinding system can be obtained:

$$\ddot{r} - \frac{\dot{r}}{\tau} = \frac{\dot{u}}{\tau} \tag{5}$$

where, τ is the time constant of the system, which is a measure of the relationship between the system overall effective stiffness k_e and the grinding coefficient k_c. The time constant is expressed by:

$$\tau = \frac{k_c}{k_e n_w} \tag{6}$$

The above equation shows that the time constant is related to the overall effective

stiffness k_e, the workpiece rotational speed n_w and the grinding force coefficient k_c.

The basic internal plunge grinding cycle always includes many different infeed stages, such as roughing, semi-finishing, finishing and spark-out, as shown in Fig. 2. To simulate the multi-infeed grinding behaviour, the real infeed rate $\dot{r}$ in different stages must be known.
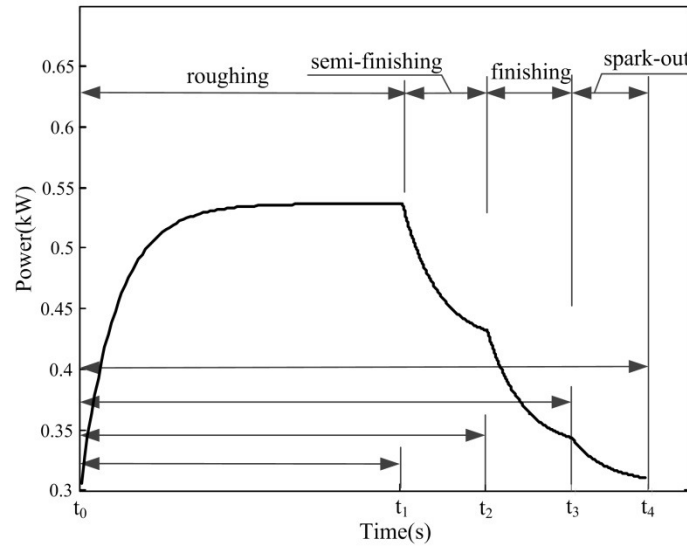

Fig. 2 Typical power curve of internal plunge grinding

For internal plunge grinding, n is used to represent the order of the infeed stage, such as roughing ($n = 1$), semi-finishing ($n = 2$), finishing ($n = 3$) and spark-out ($n = 4$), before the wheel contacts the workpiece at the initial time point ($n = 0$). As shown in Appendix B, the real infeed rate $\dot{r}(t)$ and the real workpiece radius reduction r_n of the nth infeed stage can be solved by equation (6):

$$r_n = \dot{u}_n(t-\tau) + (\dot{u}_{n-1}-\dot{u}_n)(t_{n-1}-\tau e^{-\frac{t-t_{n-1}}{\tau}}) + (\dot{u}_{n-2}-\dot{u}_{n-1})(t_{n-2}-\tau e^{-\frac{t-t_{n-2}}{\tau}})$$
$$+\cdots+(\dot{u}_1-\dot{u}_2)(t_1-\tau e^{-\frac{t-t_1}{\tau}}) + (\dot{u}_0-\dot{u}_1)(t_0-\tau e^{-\frac{t-t_0}{\tau}}) \tag{7}$$

$$\dot{r}_n(t) = \dot{u}_n + (\dot{u}_{n-1}-\dot{u}_n)e^{-\frac{t-t_{n-1}}{\tau}} +\cdots+(\dot{u}_1-\dot{u}_2)e^{-\frac{t-t_1}{\tau}} + (\dot{u}_0-\dot{u}_1)e^{-\frac{t-t_0}{\tau}} \tag{8}$$

where $\dot{u}_n$ is the commanded infeed rate of the nth infeed stage, and t_n represents the infeed time during the previous n stages, as shown in Fig. 2 ($t_n > t_{n\,1} > t_{n\,2} > \cdots > t_0$). At the start of grinding, $\dot{u}_0 = 0$ and $t_0 = 0$. Accordingly, the general relationship model for different infeed stages is established, and equations (7) and (8) can be used to study the multi-infeed stages of the internal plunge grinding process.

With an increase in the number n, calculations of equations (7) and (8) become tedious. To reduce the calculation time, for $t - t_{n-2} \gg \tau$, equations (7) and (8) can be simplified as follows:

$$r_n = \dot{u}_n(t-\tau) + (\dot{u}_{n-1} - \dot{u}_n)(t_{n-1} - \tau e^{-\frac{t-t_{n-1}}{\tau}}) + (\dot{u}_{n-2} - \dot{u}_{n-1})t_{n-2} + \cdots + (\dot{u}_0 - \dot{u}_1)t_0 \quad (9)$$

$$\dot{r}_n(t) = \dot{u}_n + (\dot{u}_{n-1} - \dot{u}_n)e^{-\frac{t-t_{n-1}}{\tau}} \quad (10)$$

3. Grinding power signal model (GPSM)

The grinding force vector can be separated into a tangential grinding force F_t and a normal grinding force F_n, as shown in Fig. 1. For internal plunge grinding, the grinding power P associated with the tangential grinding force F_t can be written as: [18]

$$P = k_p F_t v_s \quad (11)$$

where k_p is the coefficient of power, which depends on the grinding conditions, and v_s which represents the grinding wheel speed. The normal grinding force F_n is proportional to the tangential grinding force F_t:

$$F_n = k_{nt} F_t \quad (12)$$

where k_{nt} is the proportionality coefficient of the normal force and the tangential

force.

When substituting equations (8), (11) and (12) into equation (3), the power signal during the grinding process can be simulated by:

$$P = \frac{k_c k_p v_s}{k_{nt} n_w}(\dot{u}_n + (\dot{u}_{n-1} - \dot{u}_n)e^{-\frac{t-t_{n-1}}{\tau}} + \cdots + (\dot{u}_1 - \dot{u}_2)e^{-\frac{t-t_1}{\tau}} + (\dot{u}_0 - \dot{u}_1)e^{-\frac{t-t_0}{\tau}}) \quad (13)$$

According to equation (13), the proportionality coefficient $\dfrac{k_c k_p}{k_{nt}}$ and the time constant τ are generally not known. Depending on the monitoring power signal, these coefficients can be easily determined by examining the steady-state power P' as well as the rate of power change $\dot{P}$ reached in one time constant τ (τ is generally on the order of one second in precision grinding).

$$P = P' \approx \frac{k_c k_p v_s \dot{u}_n}{k_{nt} n_w} \equiv K_S \qquad (t - t_{n-1} \gg \tau) \qquad (14)$$

$$\dot{P} = \frac{k_c k_p v_s}{k_{nt} \tau n_w}(\dot{u}_n - \dot{u}_{n-1})e^{-1} \equiv \frac{K_S\left[(1 - \dfrac{u_{n-1}}{u_n})e^{-1}\right]}{\tau}(t - t_{n-1} = \tau, t - t_{n-2} \gg \tau) \quad (15)$$

Equations (14) and (15) can be applied to grinding power data to periodically update the empirical values of τ and K_S to maintain an accurate material removal prediction [9]. Once τ and K_S are known, the removed material may be quickly predicted by solving for the grinding contact time t_{grind} using equation (13):

$$t_{grind} = \tau\left(\frac{(\dot{u}_{n-1} - \dot{u}_n)e^{\frac{t_{n-1}}{\tau}} + \cdots + (\dot{u}_1 - \dot{u}_2)e^{\frac{t_1}{\tau}} + (\dot{u}_0 - \dot{u}_1)e^{\frac{t_0}{\tau}}}{\dot{u}_n(\dfrac{P}{K_S} - 1)}\right) \qquad (16)$$

where the time constant τ can be estimated using the experimental power signal data.

Finally, the prediction of the material removed is performed using equation (17).

$$r_n^{grind}(t) = \dot{u}_n(t_{grind} - \tau) + (\dot{u}_{n-1} - \dot{u}_n)(t_{n-1} - \tau e^{-\frac{t_{grind} - t_{n-1}}{\tau}})$$
$$+ \cdots + (\dot{u}_1 - \dot{u}_2)(t_1 - \tau e^{-\frac{t_{grind} - t_1}{\tau}}) + (\dot{u}_0 - \dot{u}_1)(t_0 - \tau e^{-\frac{t_{grind} - t_0}{\tau}})$$

(17)

If $t - t_{n-2} \gg \tau$, then equation (17) can be simplified by:

$$r_n^{grind}(t) = \dot{u}_n(t_{grind} - \tau) + (\dot{u}_{n-1} - \dot{u}_n)(t_{n-1} - \tau e^{-\frac{t_{grind} - t_{n-1}}{\tau}}) + (\dot{u}_{n-2} - \dot{u}_{n-1})t_{n-2}$$
$$+ \cdots + (\dot{u}_1 - \dot{u}_2)t_1 + (\dot{u}_0 - \dot{u}_1)t_0$$

(18)

As mentioned above, a general prediction model for multi-infeed internal plunge grinding is established. Compared with similar previous work [8,12,16], the general model (**GPSM**) uses all of the elastic deformation of the previous infeed stages in the current infeed stage simulation, as shown in polynomial equations (13), (16) and (17), especially when the stage ($t - t_{n-1}$ to $t - t_0$) cannot be neglected. Because the **GPSM** does not neglect the effectiveness of the previous infeed stages, it is more accurate to simulate and predict the multi-infeed internal plunge grinding. The following experiments demonstrate the utility of the model in the **BORW** internal grinding process.

4. Experimental configuration

The above theoretical method was verified experimentally using the **BORW** grinding machine described in this section. As shown in Fig. 3, the **VOLF3MZ1410 CNC** internal plunge grinding machine equipped with the grinding electric spindle, the workpiece and the dressing tool are used to process the bearing outer ring workpiece. The workpiece was installed on a centreless electromagnetic chuck. In the factory production line, the power signal of electric spindle is used to study the

BORW internal plunge grinding process. The electric spindle power was measured using a power sensor **LOAD CONTROL PH-3A** installed in a machine tool electrical cabinet. The power signal is filtered and digitised using a **DATAQ INSTRUMENTS DI-148U** data acquisition card.
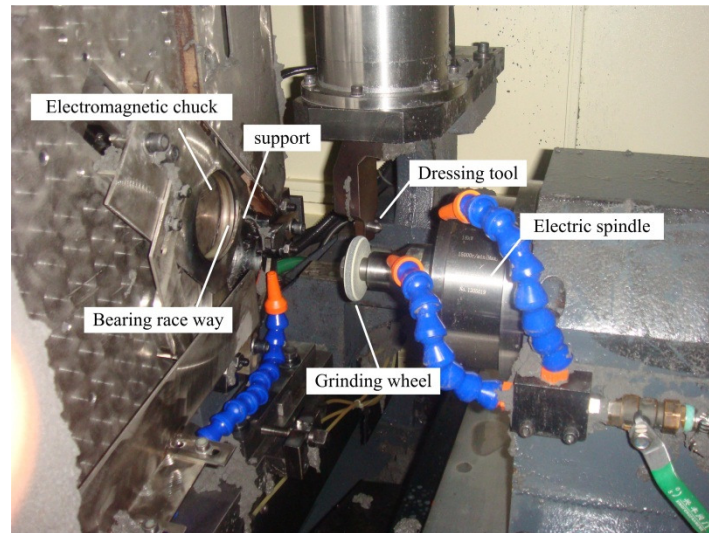

Fig. 3 Experimental setup

The parameters of the grinding wheel and the workpiece are shown in Table 1

Table 1 The parameters of the grinding wheel and the workpiece

Parameter	Property
Workpiece material	GCr15
Wheel material	Vitrified aluminium oxide
Workpiece dimension (mm)	Φ75.2 (diameter) × 12.5 (width) × Φ68.5 (race way)
Wheel dimension (mm)	Φ60 (diameter) × 7 (width) × Φ16 (bore)
Workpiece speed (r/min)	250
Wheel speed (m/s)	38

To study the multi-infeed stages of **BORW** internal plunge grinding, many tests were performed in the production line. Typically, the roughing, semi-finishing, finishing and spark-out stages are included in the **BORW** plunge grinding process. The operational parameters are given in Table 2.

Table 2 The parameters of **BORW** internal plunge grinding

Infeed stage	Grinding allowance (mm)	Infeed speed (mm/s)	Grinding time (s)

Roughing	b_{rough}=0.315	$\dot{u}_{rough}$=0.040	t_{rough}=7.87
Semi-finishing	b_{semi}=0.040	$\dot{u}_{semi}$=0.020	t_{semi}=2.00
Finishing	b_{finish}=0.010	$\dot{u}_{finish}$=0.005	t_{finish}=2.00
Spark-out	b_{spark}=0.000	$\dot{u}_{spark}$=0.000	t_{spark}=1.80

Dressing involves the establishment of both the shape and the cutting ability of the grinding wheel. The dressing tool for the grinding wheel was a single-point diamond. Every grinding three cycles, the automated dressing process is performed with dressing depth 10 µm and dressing lead 18.6 µm. As shown in Fig. 4 (a), the measured cycle power signal can be clearly recognised for all of the infeed stages, i.e., roughing, semi-finishing, finishing and spark-out. The power signals were measured from three continuous grinding cycles after dressing under the parameters shown in Table 2 (Fig. 4(b)).
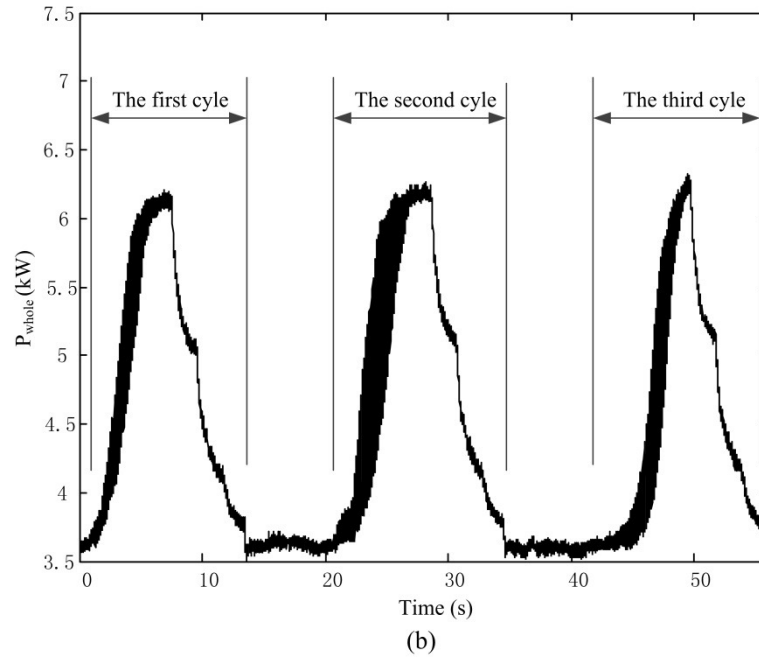

(a)
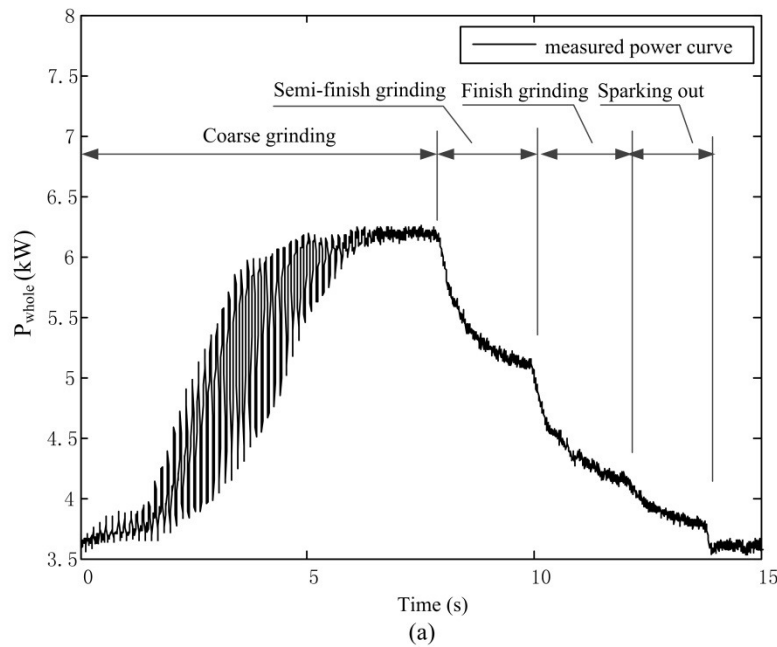
Fig. 4 **BORW** internal plunge grinding cycles: (a) one grinding cycle and (b) three grinding cycles

5. Results and discussion

This discussion is divided into three parts based on the experimental work. First, the experimental data were collected to predict the power curve. Compared with the actual grinding process, the significant error is investigated using the roughing stage and the spark-out stage, and the main influencing factors are determined. Second, a useful practical method is proposed to improve the model to predict more accurately the power curve and verify the practicality of **GPSM** for multi-infeed internal plunge grinding. Finally, an estimation of the grinding wheel performance and the grinding quality using **GPSM** coefficients is presented. The results demonstrated that **GPSM** is valuable for monitoring and analysing grinding wheel performance and grinding quality.

5.1 Prediction of the grinding power based on GPSM

To ensure the availability of the **GPSM**, three continuous grinding cycles after dressing were used to investigate the actual grinding process with the predicted power

curve. According to the whole monitoring power P_{whole}, the spindle idle power P_{idle} is approximately 3.58 **kW,** as shown in Fig. 4. The consumption power of the grinding process is equal to the difference between the whole monitoring power and the spindle idle power, which is given by:

$$P_{grind} = P_{whole} - P_{idle} \tag{19}$$

where P_{grind} is the consumption power of grinding process. For convenience of the calculation, the grinding consumption power P_{grind} is used in this section.

5.1.1 Prediction of the grinding power

The **GPSM** model described in the previous sections can be used to analyse the **BORW** internal plunge grinding process. According to equations (16) and (17) and the data in Table 2, the observed value of the coefficient K_s is directly related to the steady state of the grinding power, while the time constant τ is a function of the system compliance and material removal rates [9]. As a key variable in the proposed **GPSM**, the time constant τ should be estimated exactly. Depending on the actual power signal changing characteristics, the semi-finishing stage (n=2) power signal is selected to calculate the time constant τ using equation (15). To reduce the effect of measuring noise, the least-mean-squares (LMS) estimation method is applied to each power signal sample and is adjusted in real time. A portion of the infeed LMS power data was selected to calculate the time constant. A flow chart for the determination of the **GPSM** coefficients is presented in Fig. 5. The entire grinding cycle power curve is predicted using equation (13), as shown in Fig. 6.
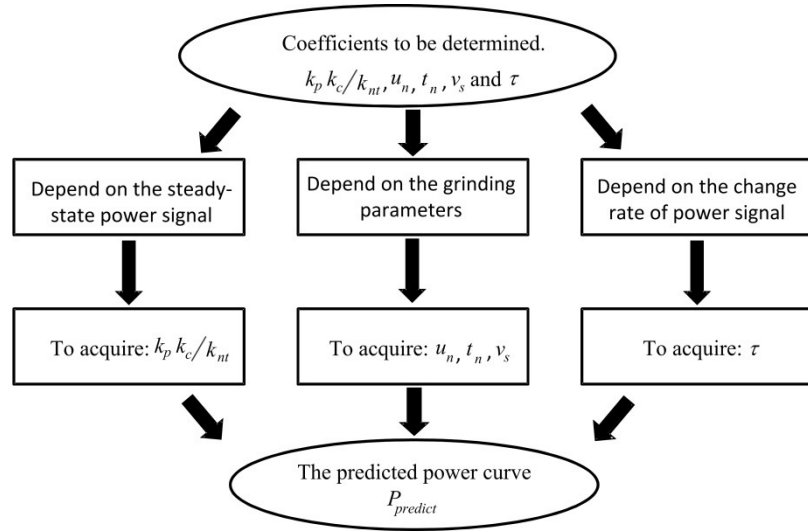
Fig. 5 Flow chart for the determination of the **GPSM** coefficients

However, in a actual internal plunge grinding process, interference due to changes in certain factors, such as the coolant drag force, thermal error, and structure system vibration, may generate significant errors. A comparison between the predicted and the measured power curves is shown in Fig. 6. The predicted power curve is not entirely consistent with the measured curve, especially for the roughing stage and the spark-out stage; these deviations are investigated in sections 5.1.2 and 5.1.3.

(a)
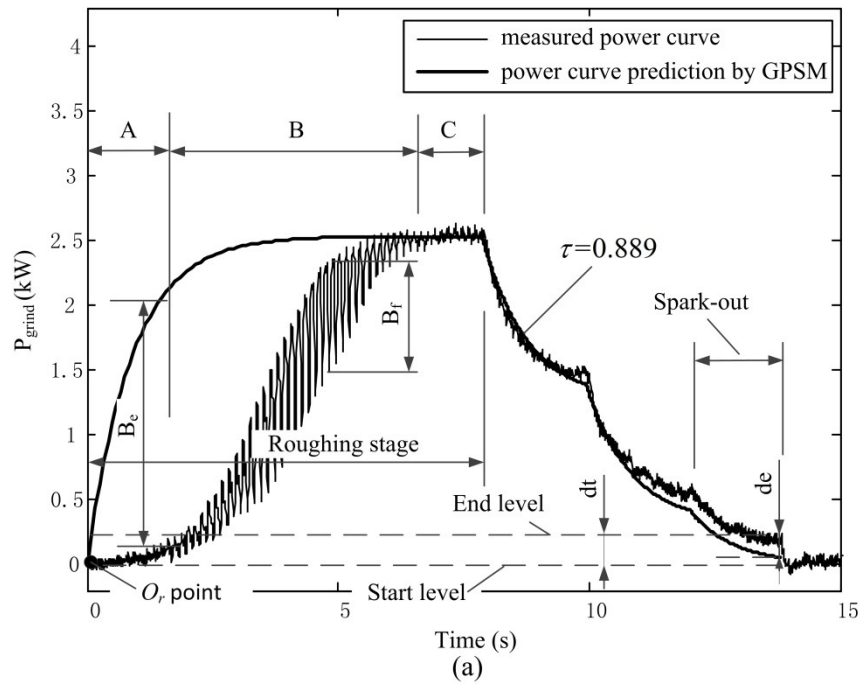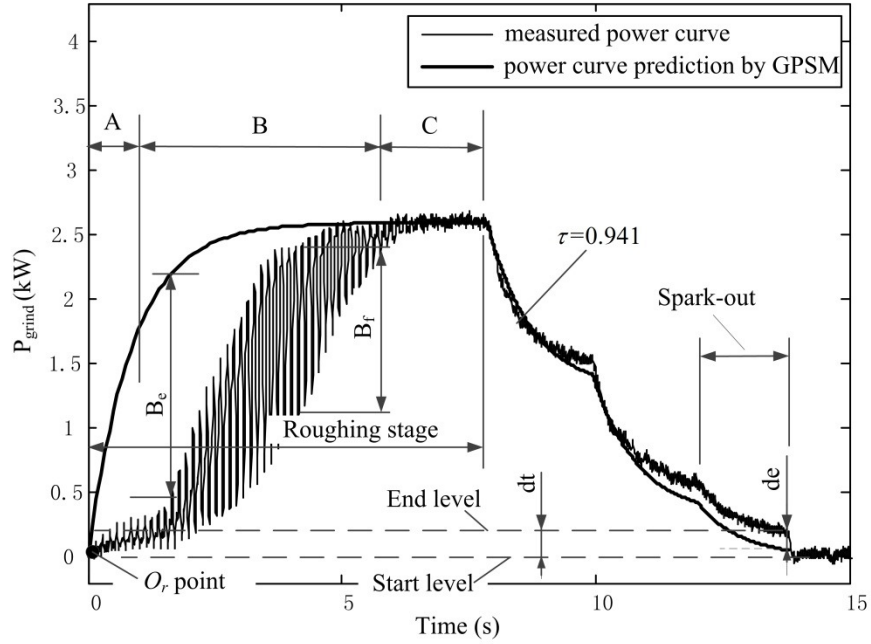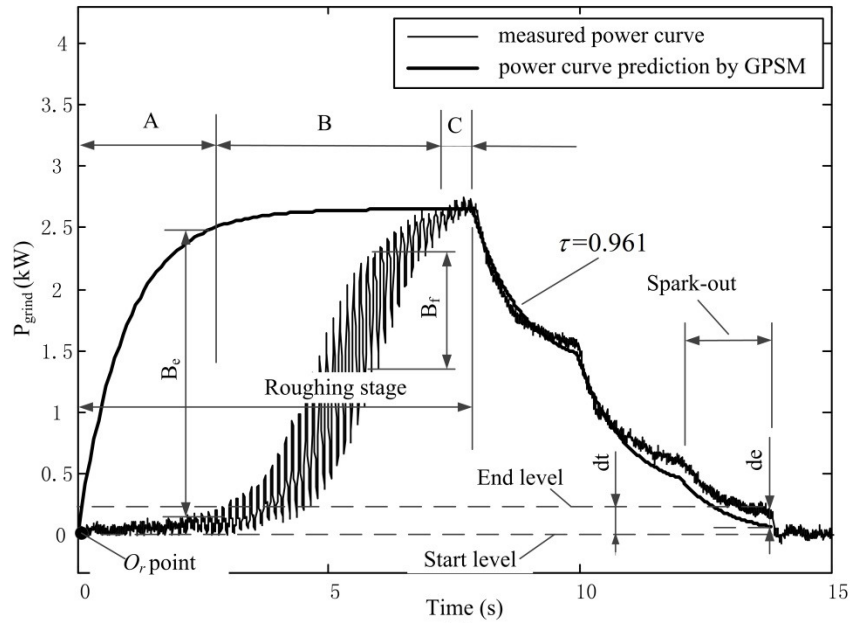
Fig. 6 Comparison between the predicted and measured power curves: (a) the first cycle, (b) the second cycle, and (c) the third cycle

5.1.2 The deviation in the roughing stage

In the roughing stage of the actual grinding process, the measured power is obviously higher than the predicted power at the beginning, as shown in Fig. 6. In addition, B_e represents the maximum deviation between the predicted and the measured power curve, in which the values are also different for the three grinding

cycles. When the measured power signal is increasing at the roughing stage, there is a severe fluctuation in the magnitude of the power, represented by B_f. Finally, the measured power signal becomes flat and close to the predicted power curve at the end of roughing stage, and the fluctuation is almost negligible.

According to the **BORW** internal plunge grinding process, the workpiece blanks are produced through heat treatment after turning, and thus, the bearing outer race way of the workpiece blanks before grinding are not part of a regular cycle, as shown in Fig. 8. Here, the typical roughing infeed stage can be divided into three stages (**A**, **B** and **C**), as shown in Figs. 6 and 7. The distance of stages **A**, **B** and **C** can be expressed by equation (20).
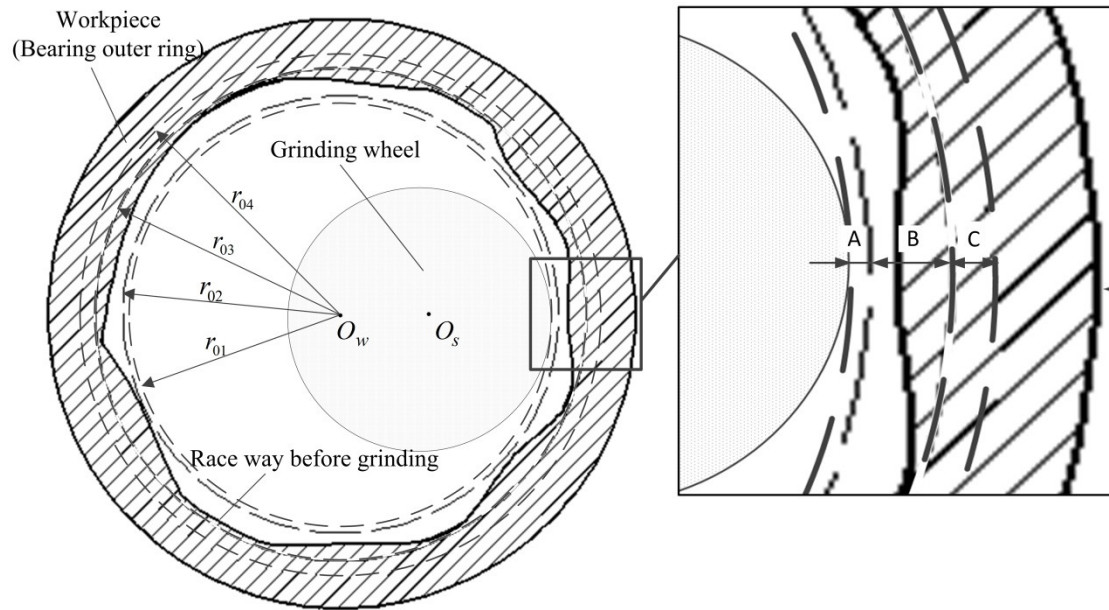

Fig. 7 **BORW** roughing process

$$l_A = r_{02} - r_{01}$$
$$l_B = r_{03} - r_{02} \qquad (20)$$
$$l_C = r_{04} - r_{03}$$

Stage **A** is the safety distance without contact between the grinding wheel and the workpiece. Due to the hydrodynamic force, the grinding power begins to increase

slowly when the wheel approaches the workpiece, which leads to a large difference relative to the predicted power curve. Because the size of the workpiece blanks is variable, the deviation value B_e is different in the three continuous grinding cycles. For stage **B**, when the grinding wheel contacts the workpiece, the irregular form is removed gradually. Due to the unstable contact between the grinding wheel and the irregular form surface, there is an obvious fluctuation in the measured power, and the grinding power fluctuation (see stage **B** in Fig. 6) changes periodically. During stage **C**, the irregular form is mostly removed, and thus, the measured power curve is close to the predicted curve.

5.1.3 The deviation in the spark-out stage

As shown in Fig. 6, the "start level" dashed line represents the measured power consumption at the beginning of the roughing stage, and the "end level" dashed line represents the measured power consumption at the end of the spark-out stage. Obviously, the end level is higher than the start level, mainly due to the coolant drag force and the residual system deformation force [8, 14], and the difference, shown as dt , is approximately 0.192 **kW** in this experiments. Because the **GPSM** predicted power curve is calculated from the Or point, which is the crossing point between the start level dash line and the measured power curve, there is a discrepancy between the end level of the measured power and the **GPSM**-predicted power, which is given by the value de of approximately 0.1375 **kW**.

The coolant drag force is produced under a steady flow of coolant between the grinding wheel and the workpiece. Depending on the machine tool operator's experience, the coolant drag force is always much larger than the residual system

deformation force. As a result, the difference between the predicted and the measured power curve during the spark-out stage is mainly generated by the coolant drag force.

Based on the aforementioned roughing and spark-out stage analysis, the significant error between the predicted and the measured power curve is related to three important influence factors: the safety distance in stage **A**, the irregular form of the workpiece blank and the coolant drag force (neglecting the residual system deformation force). Because an irregular form is produced in the turning process and the heat treatment, only two factors (the safety distance in stage **A** and the coolant drag force) should be considered in the grinding process when the **GPSM** is used to predict the power curve. The following section introduces a practical method for reducing the significant error.

## 5.2 A practical method for GPSM improvement

This section introduces a useful practical method for **GPSM** improvement to more accurately predict the grinding power curve. To reduce the influence of the safety distance in stage **A** and the coolant drag force, the **GPSM** predicted power curve is calculated from the Cr point, which is the crossing point between the end level dash lines and the rising power curve, as shown in Fig. 8. The **GPSM** predicted power curve shows that the method does not consider the time of stage **A** in the simulation, and reduce the influence of the coolant drag force. Note that the grinding consumption power P_{grind} is not suitable for determining the **GPSM** coefficients via the flow chart in Fig. 5. The **GPSM** coefficients should be determined by the pure grinding power P_{pure}, which is calculated by:

$$P_{pure} = P_{whole} - P_{idle} - dt \qquad (21)$$

where dt is the difference between the end level and the start level that is generated by the coolant drag force (neglecting the residual system deformation force). In addition, the infeeding time during roughing stage t_1 should eliminate the time of stage **A** t_A as follows:

$$t_1 = t_{rough} - t_A \qquad (22)$$

According to the practical method, the **BORW** internal plunge grinding cycle power curve is predicted as shown in Fig. 8. From the comparison between Fig. 6 and Fig. 8, the predicted power curve with the new method is clearly more consistent with the measured power signal, and the error is reduced greatly in the roughing stage and spark-out stage.
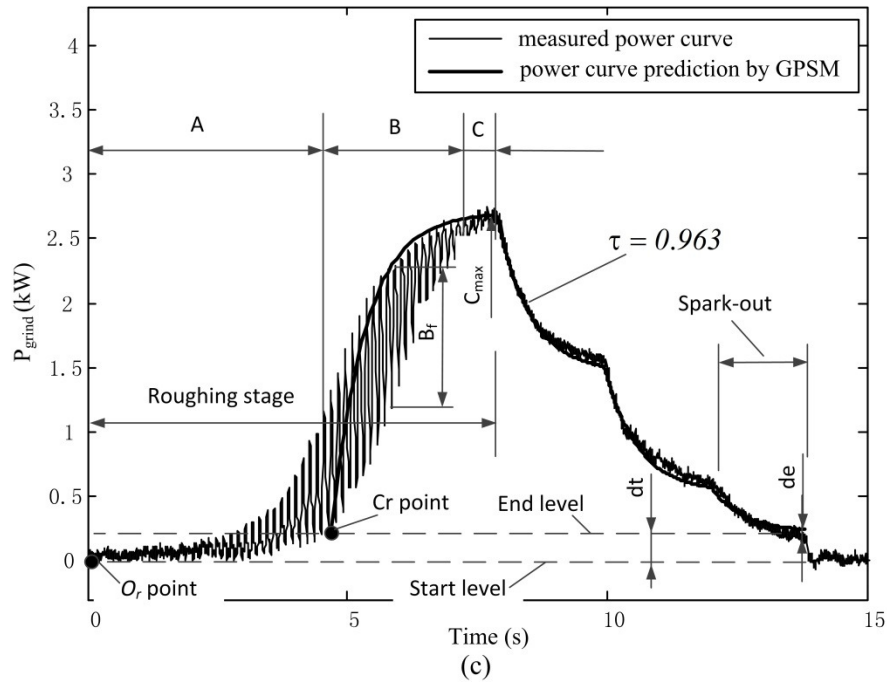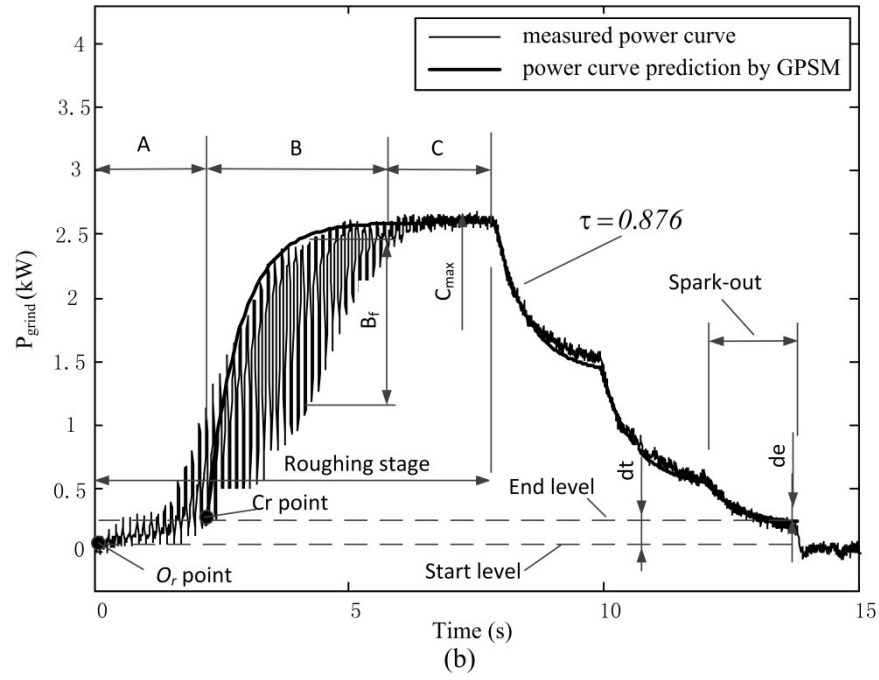

(a)
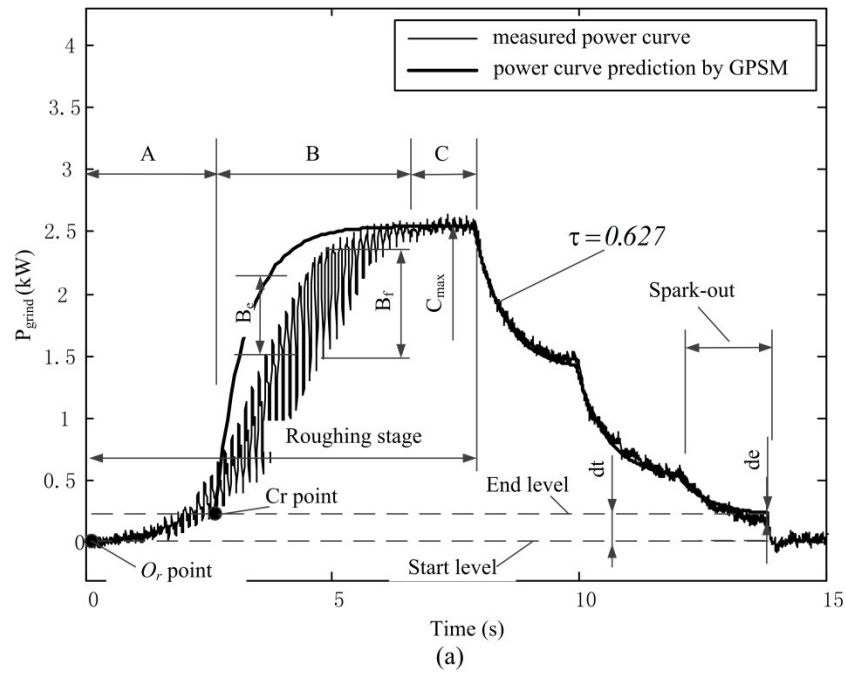
Fig. 8 Prediction of the power signal using the new method: (a) the first cycle, (b) the second cycle, and (c) the third cycle

For the roughing stage, as shown in Fig. 8, the material removal is considered to occur from the Cr point using the new method. The predicted power during the roughing stage **B** is almost coincident with the upper range of the measured power fluctuation, and the results are in agreement with the expected behaviour that the

grinding force or power is higher as more material is removed. However, a significant error B_e still exists in the first grinding cycle because the time constant τ changes rapidly at the beginning of the grinding process after the wheel has been dressed. During the grinding process, the time constant becomes stable, and the error is reduced, as observed in the second and the third cycle.

For the spark-out stage, the error de is greatly reduced to 0.0342 **kW** with the new method; this result confirmed the capability of the **GPSM** to predict the power curve for the multi-infeed internal plunge grinding process. Although a small error may be caused by the nonlinear relationship between the grinding force and the infeed rate or by the residual system deformation force, the predicted results are acceptable for use in a production line to analyse the grinding process.

5.3 Analysis of the BORW grinding process based on the improved GPSM

According to the improved **GPSM**, it is possible to determine the relationship between the predicted power and the experimental results. The estimation of the grinding wheel performance and grinding quality using **GPSM** coefficients is introduced in the following section.

5.3.1 Estimation of the grinding wheel performance using the time constant

The grinding wheel performance is an important aspect of the grinding process. The grinding wheel should be kept sharp enough to meet the requirements of the bearing parts. However, the wheel performance may change significantly during the internal plunge grinding process. It is necessary to predict the grinding wheel performance in advance and to redress the wheel when necessary.
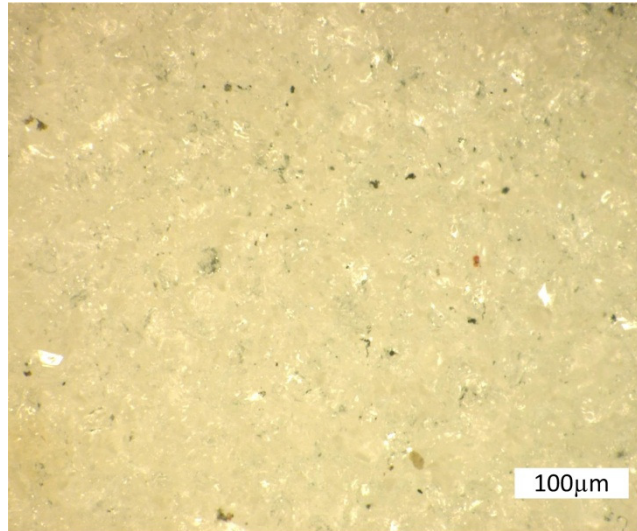
Fig. 9 The wheel surface after dressing

Direct measurement of the wheel wear is difficult during the machining process. Based on the improved **GPSM**, the time constant τ is related to the grinding force coefficient, which could be used to establish the relationship between the time constant and the wheel performance. Fig. 9 shows a clear surface of the grinding wheel after dressing. The increase of the time constant τ with consecutive grinding cycles was calculated based on the semi-finishing power signal, as shown in Figs. 10, 11 and 12; the time constant τ is 0.627 for the first cycle, 0.876 for the second cycle and 0.963 for the third cycle. The increase of the time constant value with three consecutive grinding cycles could indicate that wheel surface deterioration occurs in the process represented by the wheel loading. Therefore, it is possible to evaluate the wheel performance based on the time constant and set the limit value of the time constant to automatically control the dressing to ensure a good grinding wheel performance.
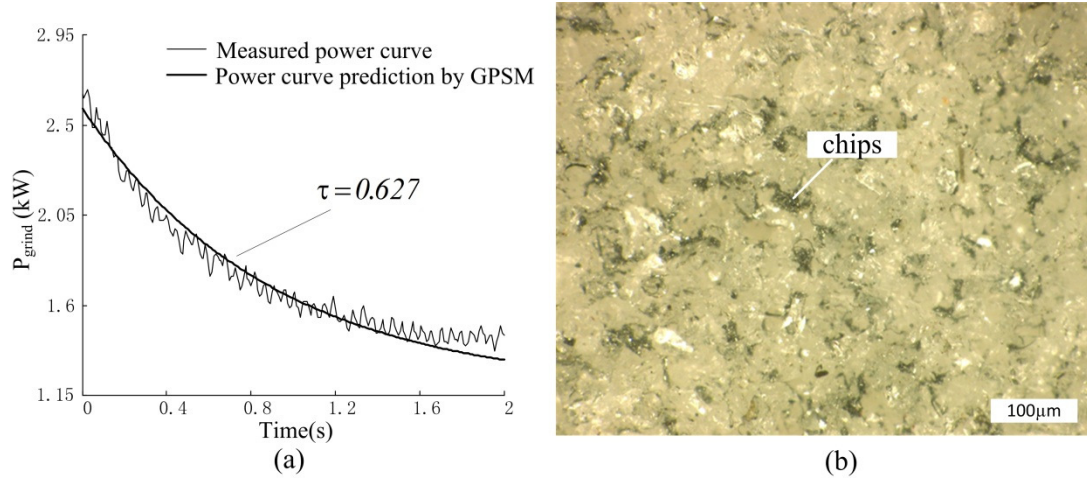
Fig. 10 Relationship between (a) the time constant value and (b) the wheel surface after the first cycle
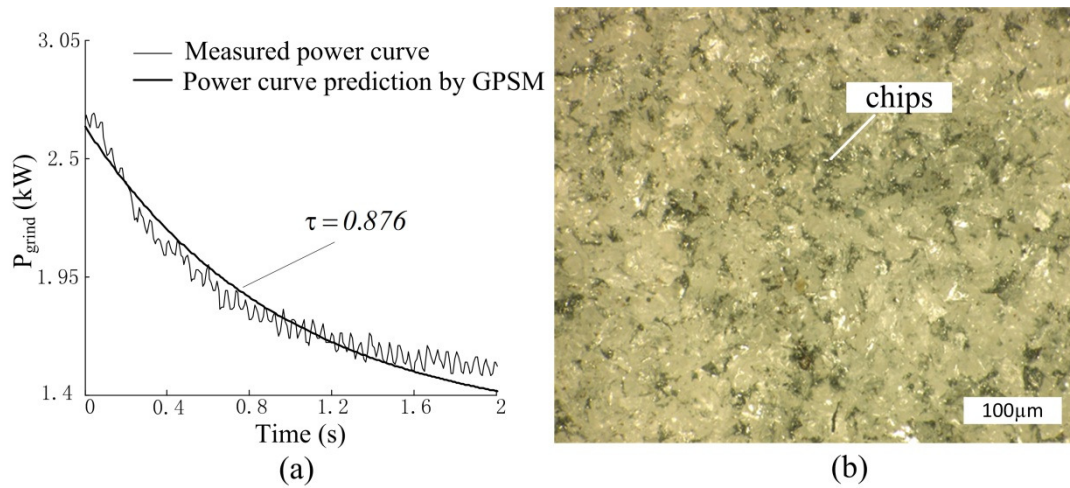

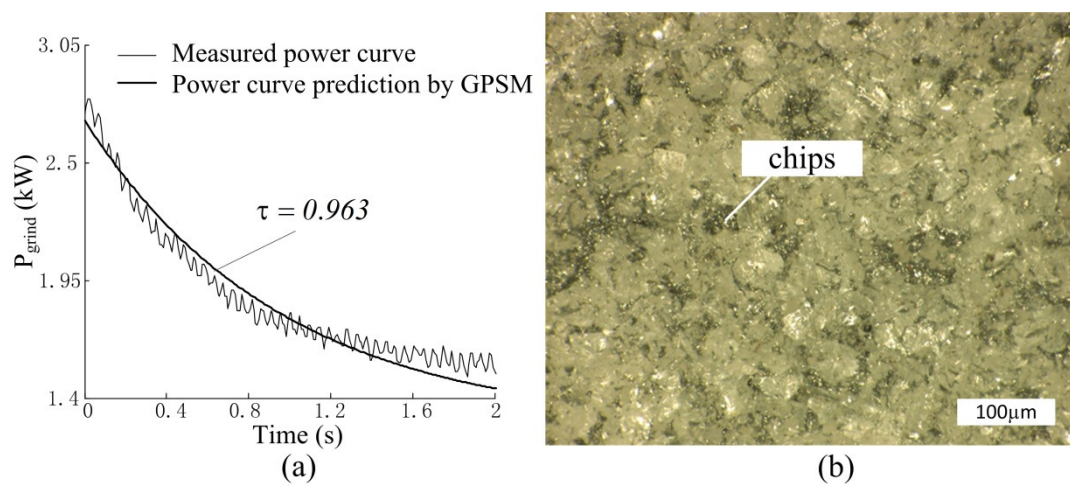Fig. 11 Relationship between (a) the time constant value and (b) the wheel surface after the second cycle

Fig. 12 Relationship between (a) the time constant value and (b) the wheel surface after the third cycle

5.3.2   Relationship between the grinding quality and the final error $\det T$

In **BORW** internal plunge grinding, the predicted wheel infeed always lags behind the commanded material removal by an amount inversely proportional to the stiffness of the grinding system [10]. As shown in Fig. 13, transient deflections are generated at the beginning of the roughing stage. Subsequently, as the rough grinding reaches a steady state, and the deflection does not change. During the finishing and spark-out stages, the deflection is close to the commanded deflection. Due to the system residual deformation, there is still some error between the predicted workpiece size and the target size at the end of spark-out stage, and the final error is defined as $\det T$. The relationship between the grinding quality and the $\det T$ value is presented below.
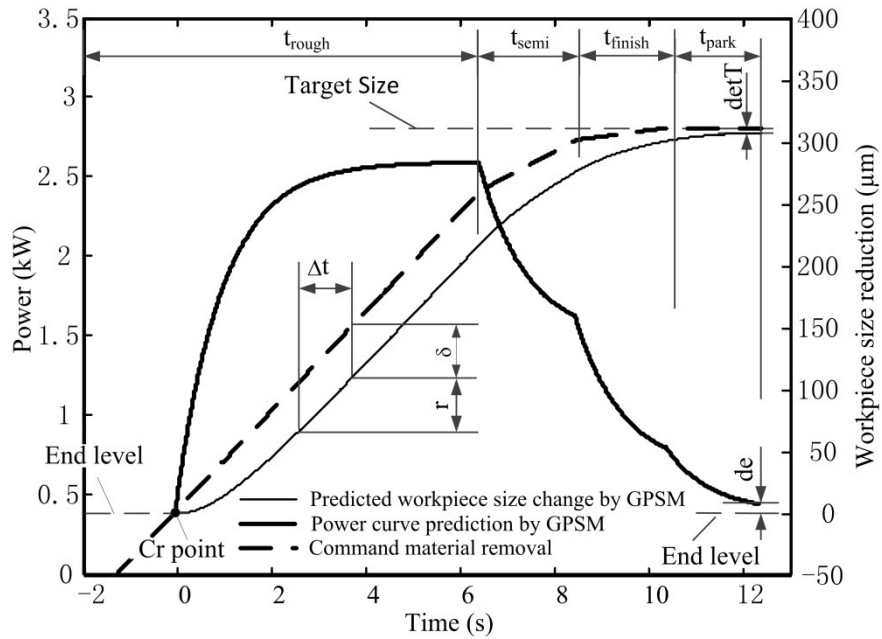

Fig. 13 **BORW** internal plunge grinding cycle

Fig. 14 shows the **BORW** roughness measurement of three consecutive grinding workpieces using a contour graph. Fig. 15 illustrates the relationship between the surface roughness and the final error $\det T$ in three consecutive grinding cycles. The experimental results show that the roughness of the grinding workpiece increases

with the final error $\det T$, and the $\det T$ values were 3.80 µm for the first cycle, 3.932 µm for the second and 4.022 µm for the third cycle.

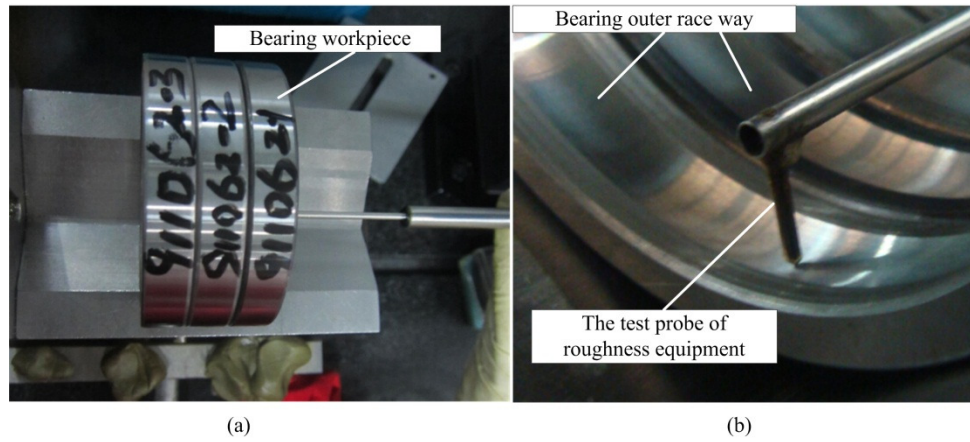(a)   (b)

Fig. 14 Roughness measurement: (a) three bearing workpieces and (b) measurement process
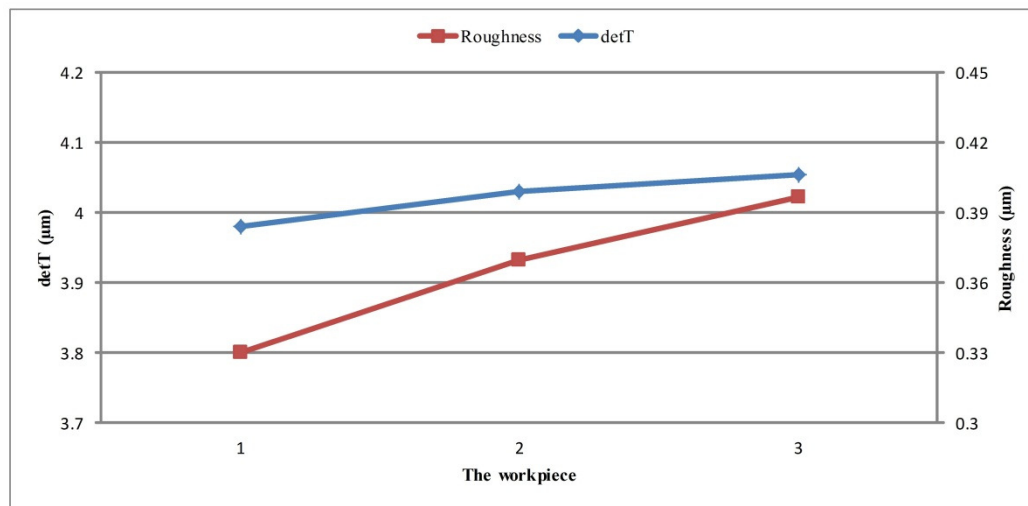
Fig. 15 Relationship between the roughness and det T

Fig. 16 shows the roundness measurement of three continuous workpieces, and the result of the wave range (2~15) is used as the main roundness index to describe the grind quality. Fig. 17 shows the correlated roundness as well as the final error $\det T$ relative to the continuous grinding workpieces under the same parameters. The figure also shows that the roundness values also increase with the final error $\det T$ in the three consecutive grinding cycles.
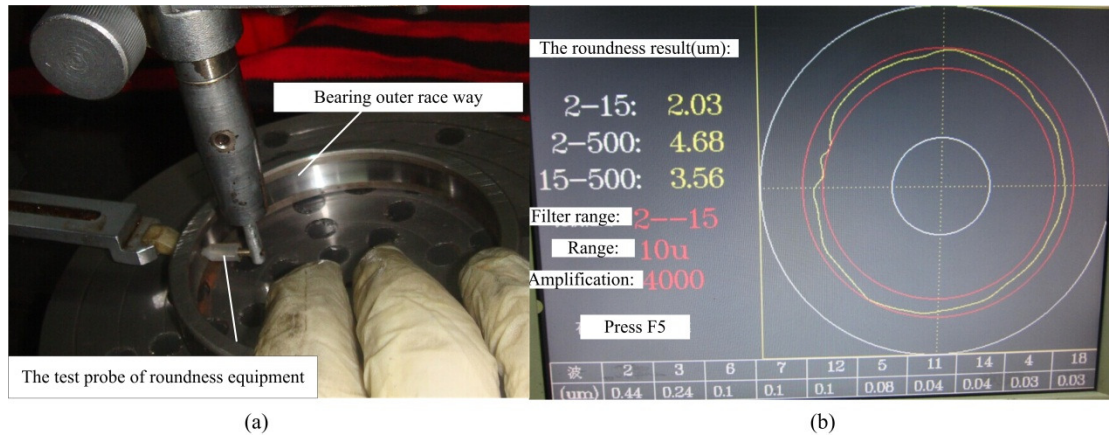
Fig. 16 Roundness measurement: (a) measurement process and (b) the roundness result
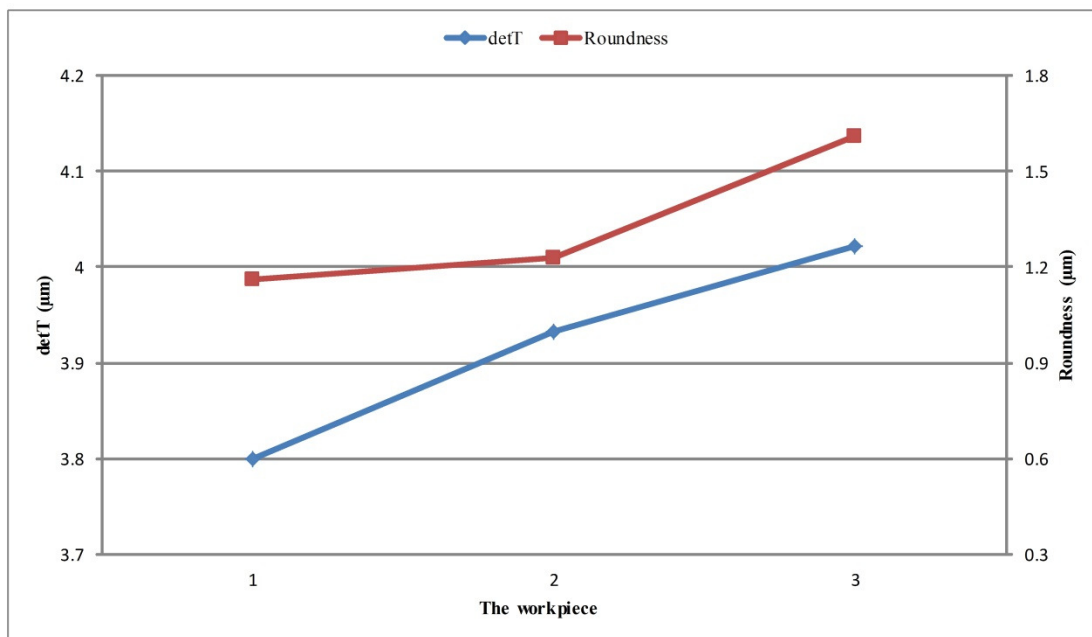
Fig. 17 Relationship between the roundness and det T

The test was performed using different process parameters, and the results could be consistently reproduced. The proportional behaviour between the workpiece quality (roughness and roundness) and the **GPSM** coefficients (τ and $\det T$) is presented, and the results are critical for optimising and controlling the **BORW** grinding process. To improve the workpiece quality, it is necessary to maintain the time constant and the final error $\det T$ below a certain limit value during the actual grinding process.

6. Conclusion

For **BORW** internal plunge grinding with multi-infeed stages (such as roughing, semi-finishing, finishing and spark-out), the general model (**GPSM**) presents obvious advantages in an actual factory for monitoring the entire process based on the power signal. The following conclusion can be drawn:

1) A general model for multi-infeed internal plunge grinding is established. The general model (**GPSM**) considers all of the elastic deformation of the previous infeed stages into the current infeed stage prediction, and the model more accurately predicts the multi-infeed internal plunge grinding, especially when the deformation of the previous infeed stages cannot be neglected.

2) Many experiments were performed to predict the power curve and verify the applicability of **GPSM** for a multi-infeed internal plunge grinding process. As a key variable in the proposed **GPSM**, the time constant is determined using the semi-finishing stage (n=2) power signal based on the least-mean-squares (LMS) estimation method. A flow chart for **GPSM** coefficient determination is proposed in Fig. 5.

3) Compared with the actual grinding process, the significant error between the measured power curve and the predicted curve is investigated using the roughing stage and the spark-out stage. The main influencing factors can be determined, i.e., the idle stage **A**, the irregular deformation of the workpiece blank and the coolant drag force. Finally, a useful practical method for **GPSM** improvement is proposed to predict more accurately the grinding power curve.

4) According to the improved **GPSM**, estimations of grinding wheel performance

and grinding quality using **GPSM** coefficients are also presented. The results show that there is a proportional behaviour between the time constant and the grinding wheel performance. The material removal monitoring method could be deployed to analyse the grinding process and improve the grind quality.

In addition to grinding process monitoring and analysis, another important aspect of **GPSM** is that it can be used to automatically optimise the grinding parameters in terms of the total grinding time or total grinding cost. The grinding optimisation process will be studied in detail in future work.

Conflict of interest

None declared.

References:

[1] H Y Kim, S R Kim, J H Ahn, et al. Processing monitoring of centerless grinding using acoustic emission. *Journal of materials processing technology* 2011; 11: 273-278.

[2] Cheol W Lee. A control-oriented model for the cylindrical grinding process. *Int J Adv Manuf Technol* 2009; 44: 657-666.

[3] Berend Denkena, Tobias Ortmaier, Markus Ahrens, et al. Monitoring of grinding wheel defects using recursive estimation. *Int J Adv Manuf Technal* 2014; 75: 1005-1015.

[4] Yongsheng Gao, Barrie Jones. Fast time constant estimation for plunge grinding process control. *International Journal of Machine Tools & Manufacture* 1999; 39: 143-156.

[5] T Warren Liao, Chi-Fen Ting, J Qu, et al. A wavelet-based methodology for grinding wheel condition monitoring. *International Journal of Machine Tools & Manufacture* 2007; 47: 580-592.

[6] Jae-Seob Kwak, Sung-Bo Sim, Yeong-Deug Jeong. An analysis of grinding power and surface roughness in external cylindrical grinding of hardened SCM440 steel using the response surface method. *International Journal of Machine Tools & Manufacture* 2006; 46: 304-312.

[7] Y Gao, X Huang, Y Zhang. An improved discrete system model for form error control in surface grinding. *Journal of materials processing technology* 2010; 210: 1794-1804.

[8] Marsh ER, Moerlein AW, Deakyne TRS and Doren MJV. In-process measurement of form error and force in cylindrical-plunge grinding. *Precis Eng* 2008; 32: 348–352.

[9] Alex W Moerlein. In-process force measurement for diameter control in presion cylindrical grinding. *Int J Adv Manuf Technol* 2009; 42: 93-101.

[10] T Jayakmar, C K Mukhopadyay, S Venugpal, et al. A review of the application of acoustic emission techniques for monitoring forming and grinding processes. *Journal of Materials Processing Technology* 2005; 159: 48-61.

[11] Chen Jiang, Haolin Li, Yunfei Mai and Debao Guo. Material removal monitoring in precision cylindrical plunge grinding using acoustic emission signal. *Proceedings of the Institution of Mechanical Engineers, Part C: Journal of Mechanical Engineering Science* 2014; 228: 715-722.

[12] Chen Jiang, Qi Song, Debao Guo and Haolin Li. Estimation algorithm of minimum dwell time in precision cylindrical plunge grinding using acoustic emission signal. *International journal of precision engineering and manufacturing* 2014; 15(4): 601-607.

[13] Tawakoli T. Developments in grinding process monitoring and evaluation of results. *Int J Mech Manuf Syst* 2008; 1(4): 307-320.

[14] Axinte D, Gindy N. Assessment of the effectiveness of a spindle power signal for tool condition monitoring in machining processes. *Int J Prod Res* 2004; 42: 2679-2691.

[15] Xun Chen, D Allanson, A Thomas, et al. Simulation of feed cycles for grinding between centers. *Int.J.Mach.Tools Manufact* 1994; 34: 603-616.

[16] Chen X, Rowe WB, Mills B, et al. Analysis and simulation of the grinding process. Part III. Comparison with experiment. *Int J Mach Tools Manuf* 1996; 36(8): 897–906.

[17] R S Hahn. Controlled-force grinding-a new technique for precision internal grinding. *ASME J.Engng in* 1964; 86: 287-293.

[18] Eun-Sang Lee, Jeong-Du Kim, Nam-Hun Kim. Plunge grinding characteristics using the current signal of spindle motor. *Journal of Materials Processing Technology* 2003; 132: 58-66.

Appendix A

Notation

a instantaneous depth of the cut per workpiece revolution

B_f the measured power signal fluctuation magnitude

B_e the maximum deviation between the predicted and measured power curves

Cr the crossing point between the end level dashed lines and the measured power curve

de the discrepancy between the end level of the measured power and the predicted curve

dt the difference between the end level and the start level

F_n normal grinding force

F_t tangential grinding force

k_a contact stiffness between grinding wheel and workpiece

k_c grinding coefficient

k_e overall effective stiffness

k_{nt} proportionality coefficient of the normal force and the tangential force

k_p coefficient of power

k_s grinding wheel stiffness

k_w workpiece stiffness

n_w workpiece rotational speed

Or the crossing point between the start level dash lines and the measured power curve

O_S grinding wheel centre

O_W workpiece centre

P grinding power

P' steady-state power

$\dot{P}$ the rate of power change

P_{grind} consumption power of the grinding process

P_{idle} spindle idle power

P_{pure} pure grinding power

P_{whole} whole monitoring power

r real workpiece radius reduction

$\dot{r}$ real infeed rate

r_n^{grind} prediction of material removal

t_{grind} grinding contact time

$\dot{u}$ commanded infeed rate

v_s grinding wheel speed

v_w workpiece speed

δ radial elastic deflection

τ time constant

Appendix B

Derivation of equation (7) using equation (6) .

The recursive identification method is used to prove that equation (7) is the general term solution of equation (6).

According to the constant coefficient non-homogeneous linear differential equation, the solution of equation (6) is:

$$r(t) = C_1 e^{-\frac{t}{\tau}} + C_2 + \dot{u}t \tag{23}$$

where, C_1 and C_2 are the constant coefficients, which are determined by the boundary conditions.

In the first stage of a grinding cycle, $n=1$, the initial conditions are $r(t)\,|_{t=0}=0$ and $\dot{r}(t)\,|_{t=0}=0$. Combined with equation (23), the constant coefficients are given by:

$$\begin{cases} C_1 = \dot{u}_1 \tau \\ C_2 = -\dot{u}_1 \tau \end{cases} \tag{24}$$

where $\dot{u}_1$ is the wheel infeed rate at the first stage of a grinding cycle. The constant coefficients equation (24) may be substituted into equation (23) to obtain the material removal formula $r_1(t)$:

$$r_1(t) = \dot{u}_1(t - \tau) + (\dot{u}_0 - \dot{u}_1)(t_0 - \tau e^{-\frac{t-t_0}{\tau}}) \tag{25}$$

where $t_0 = 0$, and $\dot{u}_0 = 0$. This equation proves that the solution to equation (7) is consistent with equation (25), which is the solution of equation (6) when $n=1$.

It is assumed that equation (7) is the solution of equation (6) when $n=k$. The solution is given by:

$$r_k = \dot{u}_k(t-\tau) + (\dot{u}_{k-1} - \dot{u}_k)(t_{k-1} - \tau e^{-\frac{t-t_{k-1}}{\tau}}) + (\dot{u}_{k-2} - \dot{u}_{k-1})(t_{k-2} - \tau e^{-\frac{t-t_{k-2}}{\tau}})$$
$$+ \cdots + (\dot{u}_1 - \dot{u}_2)(t_1 - \tau e^{-\frac{t-t_1}{\tau}}) + (\dot{u}_0 - \dot{u}_1)(t_0 - \tau e^{-\frac{t-t_0}{\tau}}) \tag{26}$$

When $n = k+1$, the initial conditions are:

$$
\begin{cases}
r(t)|_{t=t_k} = \dot{u}_k(t_k - \tau) + (\dot{u}_{k-1} - \dot{u}_k)(t_{k-1} - \tau e^{-\frac{t_k-t_{k-1}}{\tau}}) + (\dot{u}_{k-2} - \dot{u}_{k-1})(t_{k-2} - \tau e^{-\frac{t_k-t_{k-2}}{\tau}}) \\
\quad + \cdots + (\dot{u}_1 - \dot{u}_2)(t_1 - \tau e^{-\frac{t_k-t_1}{\tau}}) + (\dot{u}_0 - \dot{u}_1)(t_0 - \tau e^{-\frac{t_k-t_0}{\tau}}) \\
\dot{r}(t)|_{t=t_k} = \dot{u}_k + (\dot{u}_{k-1} - \dot{u}_k)e^{-\frac{t_k-t_{k-1}}{\tau}} + (\dot{u}_{k-2} - \dot{u}_{k-1})e^{-\frac{t_k-t_{k-2}}{\tau}} \\
\quad + \cdots + (\dot{u}_1 - \dot{u}_2)e^{-\frac{t_k-t_1}{\tau}} + (\dot{u}_0 - \dot{u}_1)e^{-\frac{t_k-t_0}{\tau}}
\end{cases} \tag{27}
$$

Combining equations (23) and (27), the solution of constant coefficients is:

$$
\begin{cases}
C_1 = (\dot{u}_{k-1} - \dot{u}_k)\tau e^{\frac{t_k}{\tau}} + (\dot{u}_{k-2} - \dot{u}_{k-1})\tau e^{\frac{t_{k-1}}{\tau}} + \cdots + (\dot{u}_0 - \dot{u}_1)e^{\frac{t_0}{\tau}} \\
C_2 = (\dot{u}_k - \dot{u}_{k+1})t_k + (\dot{u}_{k-1} - \dot{u}_k)t_{k-1} + \cdots + (\dot{u}_1 - \dot{u}_2)t_1 + \dot{u}_{k+1}\tau
\end{cases} \tag{28}
$$

Equation (28) is substituted into equation (23) to obtain the material removal

formula $r_{k+1}(t)$:

$$r_{k+1} = \dot{u}_{k+1}(t-\tau) + (\dot{u}_k - \dot{u}_{k+1})(t_k - \tau e^{-\frac{t-t_k}{\tau}}) + (\dot{u}_{k-1} - \dot{u}_k)(t_{k-1} - \tau e^{-\frac{t-t_{k-1}}{\tau}})$$
$$+ \cdots + (\dot{u}_1 - \dot{u}_2)(t_1 - \tau e^{-\frac{t-t_1}{\tau}}) + (\dot{u}_0 - \dot{u}_1)(t_0 - \tau e^{-\frac{t-t_0}{\tau}}) \tag{29}$$

Equation (7) is proved to be consistent with equation (29) when $n = k+1$.

The above calculation demonstrates that equation (7) is the general term solution of

equation (6).